THE INTERPLAY BETWEEN ADSORPTION AND AGGREGATION OF VON WILLEBRAND FACTOR CHAINS IN SHEAR FLOWS

Helman Amaya-Espinosa [1,2], Alfredo Alexander-Katz[3], and Camilo Aponte-Santamaría[1,4,*]

[1]Max Planck Tandem Group in Computational Biophysics, Universidad de los Andes, Bogotá, Colombia.
[2]Department of Biomedical Engineering, Universidad de los Andes, Bogotá, Colombia.
[3]Department of Materials Science and Engineering, Massachusetts Institute of Technology, Cambridge, USA.
[4]Molecular Biomechanics Group, Heidelberg Institute for Theoretical Studies, Heidelberg, Germany.
*Corresponding author: camilo.aponte@h-its.org

ABSTRACT

Von Willebrand factor (VWF) is a giant extracellular glycoprotein that carries out a key adhesive function during primary hemostasis. Upon vascular injury and triggered by the shear of flowing blood, VWF establishes specific interactions with several molecular partners in order to anchor platelets to collagen on the exposed sub-endothelial surface. VWF also interacts with itself to form aggregates that, adsorbed on the surface, provide more anchor sites for the platelets. However, the interplay between elongation and subsequent exposure of cryptic binding sites, self-association, and adsorption on the surface, remained unclear for VWF. In particular, the role of shear flow in these three processes is not well understood. In this study, we address these questions by using Brownian dynamics simulations at a coarse-grained level of resolution. We considered a system consisting of multiple VWF-like self-interacting chains that also interact with a surface under a shear flow. By a systematic analysis, we reveal that chain-chain and chain-surface interactions coexist non-trivially to modulate the spontaneous adsorption of VWF and the posterior immobilization of secondary tethered chains. Accordingly, these interactions tune VWF's extension and its propensity to form shear-assisted functional adsorbed aggregates. Our data highlights the collective behavior VWF self-interacting chains have when bound to the surface, distinct from that of isolated or flowing chains. Furthermore, we show that the extension and the exposure to solvent have a similar dependence on shear flow, at a VWF-monomer level of resolution. Overall, our results highlight the complex interplay that exists between adsorption, cohesion, and shear forces and its relevance for the adhesive hemostatic function of VWF.

Introduction

When a vascular injury occurs, the subendothelium of blood vessels gets exposed and in order to stop the bleeding the hemostasis immune response is initiated. During this process, multiple thrombogenic substances interact with each other to create and stabilize a hemostatic plug. Von Willebrand factor (VWF) is among them [1, 2]. VWF anchors platelets to the sub-endothelial surface exposed by the injury[3], triggered by the shear-stress imposed by the flowing blood [4, 5, 6, 7, 8]. Accordingly, malfunction of VWF is related to a broad range of bleeding disorders [9].

VWF is a huge adhesive extracellular-protein biopolymer, with a multimeric structure of variable and exponentially-distributed length [1, 10, 11]. It is composed of multiple covalently-bound monomers, organized in a head-to-head and tail-to-tail sequence [1, 9]. Each mature VWF monomer is made up of 12 protein domains of nanometer size [1]. VWF undergoes reversible conformational changes from a globular to a stretched conformation under a flow [4, 5], thereby exposing binding sites for the interaction with a multitude of partners. Importantly, VWF attaches to the surface by establishing specific interactions with the exposed collagen of the subendothelium, via primarily the VWF A3 domain [12]. Tethered on the surface, VWF immobilizes flowing platelets, via the interaction of its A1 domain with the glycoprotein IB α platelet receptor [13, 14]. A reinforcement follows with the binding of the platelet integrin αIIbβ3 to the VWF C4 domain [7, 8].

A key concept is the ability of VWF to interact with itself. Non-covalent self-association of freely-flowing VWF chains on immobilized ones has been previously demonstrated [15, 16, 17]. A consequence of self-association was thus the enhancement of platelet adhesion by providing more binding sites, through both, directly and indirectly, immobilized VWF [18]. VWF has also been observed to bind to platelet-bound VWF, thereby promoting platelet activation [19]. Single-molecule experiments revealed that tension along the tethered chains promoted VWF elongation, which regulates the reversible self-association of VWF [20]. However, there is evidence suggesting that VWF self-associates under static conditions too [21]. Furthermore, multiple protein domains have been found to participate in the self-association of VWF [21], which is also regulated by the A2 domain [22, 23].

Specific domain–domain non-covalent self-interactions are involved in crucial functional aspects of VWF. Examples of this are the force-mediated auto-inhibition of VWF for the binding of platelets mediated by A1–A2 interactions [24, 25, 26, 27], the pH and calcium-dependent stabilization of VWF dimmers imparted by the interaction of the VWF D4 domain [28], and the assembly of VWF tubules for storage, stabilized by D–D and D–A1 interactions [29, 30, 31, 32].

VWF has been the subject of intense studies over the last three decades [1]. In particular, computer simulations have contributed enormously to the functional understanding of this protein. VWF is commonly simulated at a coarse-grained (CG) level of resolution with each CG bead representing a monomer (or a dimer). Such coarsening has enabled simulations to reach relevant spatio-temporal scales and thereby establish the link between the shear-stress imposed by the flowing blood and the elongation propensity of VWF [4]. Simulations also explained the factors governing the formation of reversible polymer-colloid VWF-platelet-like aggregates [6] and the adherence of single-VWF chains to a surface [33, 34, 35, 36], as well as the mechanism underlying enzymatic cleavage [37, 38]. CG simulations also showed that VWF adsorption obeys a cooperative mechanism [39] and added support to the involvement of D4–D4 interactions on the stability of VWF dimers [40].

Despite the wealth of this data, the interplay between three key processes of VWF, namely, elongation and subsequent exposure of cryptic binding sites; chain adsorption, and self-association, in the context of multiple chains subjected to shear flow, remains poorly understood. We addressed this issue by performing Brownian dynamics (BD) simulations of a set of VWF chains under shear flows. We adopted a bead-spring CG representation, in which each chain bead represented a VWF domain. This level of resolution, higher than conventional VWF CG models, allowed us to consider the exact distribution of domains that bind to the surface (namely the VWF A3 domains) and to retrieve more realistic surface area exposures. Our simulations demonstrate a complex interplay in which inter-chain cohesiveness and surface-chain interactions modulate the shear response of VWF chains, tuning their elongation and their propensity to form functional adsorbed aggregates. Our data highlights the different behavior VWF chains have, depending on whether they are bound to the surface or flowing. These findings also show the collective behavior VWF chains exhibit which leads to distinct properties compared to VWF chains in isolation. Finally, we studied the effect the level of resolution has on the chain exposure to the solvent and compare that with the extension, a very common descriptor of the biological function of VWF.

Methods

Coarse-grained model

Biopolymers were modeled as chains of interacting beads (Fig. 1*A*). Neighbor beads $(i, i+1)$ were bonded by harmonic springs, modeled via a potential energy

$$U_H = \frac{k}{2}\left(r_{i,i+1} - 2a\right)^2 .$$

Here, $r_{i,i+1}$ is the distance between consecutive beads, a the bead radius, and k the spring constant (a soft spring $k = 100$ kJ/mol·nm^2 was used). Volume exclusion between pairs of beads (i, j) was considered through a short-range Lennard-Jones potential

$$U_{\mathrm{LJ}} = 4\varepsilon\left[\left(\frac{\sigma}{r_{ij}}\right)^{12} - \left(\frac{\sigma}{r_{ij}}\right)^{6}\right],$$

with r_{ij} the distance between beads i and j. σ was set to $2a$, i.e. related to the minimum equilibrium separation between beads. The strength of the non-bonded interaction ϵ was normalized by the thermal energy, k_BT, with k_B the Boltzmann constant and T the temperature (k_BT ∼2.5 kJ/mol at 300 K). Accordingly, normalized values $\tilde{\epsilon} = \varepsilon/k_BT$ =0.2, 0.4, 0.6, 0.8, 1.0 were considered. This range allowed the chains to be extended by shear flows [4].

Interactions with the bottom and top surfaces of the simulation box were modeled by a 10-4 potential [41]:

$$U_w(z) = \epsilon_w\left(\frac{5}{3}\right)\left(\frac{5}{2}\right)^{\frac{2}{3}}\left[\left(\frac{\sigma}{z}\right)^{10} - \left(\frac{\sigma}{z}\right)^{4}\right].$$

Here, z is the distance from the bead to either surface. The strength of the interaction was controlled with the parameter ϵ_w. This parameter was fixed at a weak value at the top surface ($\varepsilon_w = 10^{-5}$kJ/mol, i.e. $\tilde{\epsilon}_w = \varepsilon_w/k_BT = 4\cdot10^{-6}$) to prevent accumulation of chains on this surface. The adsorption of chains at the bottom surface was of interest and therefore the interaction energy with that surface was increased ($\tilde{\epsilon}_w = 4\cdot10^{-2}$). Note that this value was varied for a specific set of beads resembling the VWF A3 domains (see below). The same σ value was used here as with the Lennard-Jones potential used between bead pairs.

To mimic VWF biopolymers, each bead was assumed to represent one VWF protein domain (i.e. $a = 1.6$ nm according to the radius of gyration obtained for the VWF

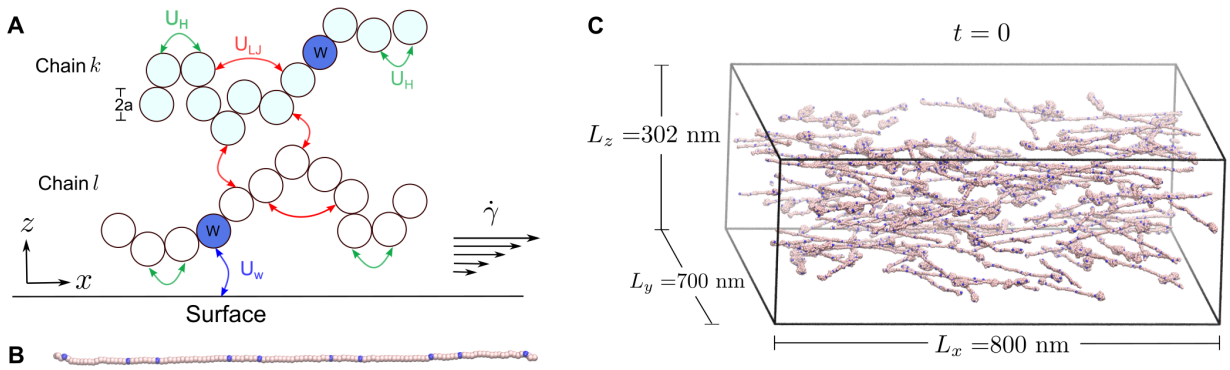

Figure 1: **Coarse-grained model to monitor the aggregation and adsorption of VWF-like biopolymers under shear flows. (A)** The scheme shows two biopolymer chains (here a VWF monomer) composed of several protein domains (circles). The size of one bead resembled the size of the VWF A1 domain ($2a = 3.2$ nm). Neighbor beads interact via bonded harmonic interactions U_H. Non-neighbor bead interactions were modeled through a short-range Lennard-Jones potential U_{LJ}, both in (here chain k) or across chains (k and l). The potential U_w takes into account the interaction of the beads with the surface. A particularly strong interaction for the bead corresponding to the VWF A3 domain (blue W-labeled bead) was considered. A shear flow with a shear rate $\dot{\gamma}$ was imposed on the chains as indicated by the arrows. **(B)** Biopolymer chains of n=120 domains, corresponding to a VWF decamer, were considered. Here a fully extended conformation of one of these chains is shown. Domains specifically interacting with the surface were distributed along the chain based on the positions of the VWF A3 domains [1] (labeled here as W and depicted as blue spheres). **(C)** Initial configuration ($t = 0$) of the simulated system consisting of 200 biopolymer chains, with different extensions and randomly-distributed positions and orientations. Simulation box dimensions are indicated.

A1 domain by molecular dynamics simulations [26]). In addition, beads corresponding to the VWF A3 domain (labeled here as W in Fig.s 1*A, B*) were assumed to have an increased and varying interaction energy with the surface ($\tilde{\epsilon}_w = \varepsilon_w/k_BT$ =2, 6, and 10), according to previously-chosen ranges [42]. We considered chains of n=120 beads, corresponding to 10 mature VWF monomers, each one of them composed of 12 protein domains [1] (Fig. 1*B*).

The receptor density on the surface, φ, was set $\varphi = 10^{-2}$ nm^{-2}, which corresponds roughly to 1 receptor in a squared area covered by one globular VWF monomer. See the results below for a justification of this density choice.

Brownian dynamics

Biopolymer dynamics was simulated with conventional Brownian Dynamics (BD) simulations. The velocity v_i of the i-th bead was described by the Langevin equation [43, 4]:

$$v_i = \frac{\partial}{\partial t}\mathbf{r}_i = -\sum_j \mu_{ij}\boldsymbol{\nabla}U_j + \boldsymbol{\xi}_i(t). \qquad (1)$$

The first term on the right-hand side represents the velocity component associated with diffusion, which depends on the total force acting on the bead ($\boldsymbol{F}_j = -\boldsymbol{\nabla}U_j$) and the mobility tensor μ_{ij}. The term $\boldsymbol{\xi}_i$ is related to the random forces exerted by the solvent molecules over each bead. $\boldsymbol{\xi}_i(t)$ satisfies the correlation function $\langle\xi_i(t)\xi_j(t')\rangle = 2k_\mathrm{B}T\mu_0\delta_{ij}\delta(t-t')$, with μ_0 being the mobility of each bead. In the free draining regime (no hydrodynamic interactions between beads, i.e. $\mu_{ij} = \mu_0\delta_{ij}$), the equation (1) can be solved numerically at discrete time steps Δt to obtain a recursive formula for the bead positions $\boldsymbol{r}_i$ in the presence of a shear flow [43]:

$$\boldsymbol{r}_i(t+\Delta t)-\boldsymbol{r}_i(t) = -\mu_0\boldsymbol{\nabla}U(t)\Delta t + \boldsymbol{R}_i(\Delta t) + v_\mathrm{flow}(\boldsymbol{r}_i)\Delta t. \qquad (2)$$

The mobility was obtained from the diffusion coefficient $\mu_0 = D_0/k_BT$. D_0 was assumed to be $1.32\cdot10^{-4}$ nm^2/ps, an estimate for the VWF A1 domain translational diffusion coefficient, obtained from molecular dynamics simulations [26]. $\boldsymbol{R}_i(\Delta t)$ is a random number drawn from a Gaussian distribution with zero mean and width $2\Delta t D_0$. v_flow is an additional velocity term to take into account the shear flow: $v_\mathrm{flow}(\boldsymbol{r}_i) = \dot{\gamma}z_i\hat{\boldsymbol{x}}$, with z_i the position of each bead along the z coordinate, and $\dot{\gamma} = du/dz$ the shear rate, i.e. the gradient of the flow velocity (u) along the z axis. Note that this third term only affects the x component of the bead velocity (Fig. 1*A*). We expressed the time-scales in terms of the characteristic diffusion time of a single bead $\tau = a^2/D_0 = 1.939\cdot10^4$ ps. Accordingly, five dimensionless shear rates were considered: $\tau\dot{\gamma}$ =0, 0.1, 0.25, 0.67, and 1.55.

Simulation details

Brownian dynamics simulations were carried out with the particle-dynamics simulation toolkit GROMACS [44] (2020.1 version). The velocity term corresponding to the shear flow described in equation (2) was included by modifying the Brownian dynamics position iteration formula

in the GROMACS source code. 200 chains were considered. Initial conformations for the chains with different extensions were considered. The 200 chains were sequentially inserted at random positions within a simulation box of dimensions $L_x = 800$ nm, $L_y = 700$ nm, and $L_z = 302$ nm (Fig. 1*C*). The box boundary conditions were defined as periodic at the x and y axes, and reflective at the z axis. The box dimensions were big enough to accommodate each biopolymer chain in a fully stretched conformation. To remove steric clashes, a steepest descent energy-minimization was carried out before the Brownian dynamics simulations. Trajectories were obtained by numerically integrating equation (2) at discrete time steps $\Delta t = 1$ ps ($\sim 5.16 \cdot 10^{-5}\tau$) over a total simulation time of of 500 μs ($\sim 2.58 \cdot 10^4\tau$). Unless stated otherwise, the first 0.1 μs ($\sim 5.16\,\tau$) were accounted as equilibration time and thus discarded from the analysis. In total, 75 trajectories were generated by systematically varying $\dot{\gamma}$, $\tilde{\epsilon}$ and $\tilde{\epsilon}_w$.

For the purpose of comparing the dynamics, a set of simulations considering only a single chain, either freely flowing or interacting with the surface were carried out, using identical simulation parameters.

Simulation analysis

The following observables of the chains were extracted from the simulations, as a function of the dimensionless shear rate $\tau\dot{\gamma}$, the inter-chain cohesion ($\tilde{\epsilon}$), and the chain adsorption ($\tilde{\epsilon}_w$) energies.

Spatial distribution

To identify bulk and adsorption regions, the distribution of the chains along the normalized coordinate $Z = z/L_z$ was evaluated (Fig. S1). Chain center of mass Z positions (Z_{COM}) were used for this purpose.

Extension

The radius of gyration (R_g) was considered as a descriptor of the extension of the chains. The time-averaged square radius of gyration $r_g^2 = \langle R_g^2 \rangle / n(2a)^2$, normalized by the mean square end-to-end extension of an ideal chain $n(2a)^2$, was computed for each chain ($\langle\rangle$ denotes average). Subsequently, the r_g^2 values of all chains were averaged in order to get a global measure of the extension, i.e. $\langle r_g^2 \rangle$. In addition, the ratio $\langle r_g^2 \rangle_{\text{tet}} / \langle r_g^2 \rangle_{\text{bulk}}$ was computed to contrast the extension of the chains that are adhered to the surface (numerator) with respect to the freely flowing bulk ones (denominator).

Adsorption and tethering

A criterion based on the chain center of mass position is not sufficient to determine if a chain is attached to the surface or not. A more strict attaching criterion was based on the position of each bead. If a bead was at a height $z \leq 2\sigma$, then the chain this bead belonged to was assumed to be attached to the surface (from here on called an "adsorbed" chain). In addition adjacent chains that were in contact with the absorbed chains (distance $\leq 2\sigma$), but not in direct contact with the surface were also monitored (denoted as "adjacent" chains). We then considered the total number of chains tethered to the surface as the sum $N_{\text{tet}} = N_{\text{ads}} + N_{\text{adj}}$, including both the number of adsorbed (N_{ads}) and adjacent (N_{adj}) chains. The mean $\langle N_{\text{tet}} \rangle = (1/T)) \int_{t_b}^{t_e} N_{\text{tet}}(t)dt$ was used as descriptor of level of adsorption, with $T = t_e - t_b$ the total duration of the simulation ($t_e \sim 2.58 \cdot 10^4\tau$) minus the initial equilibration time ($t_b \sim 5.16\,\tau$).

Aggregation

We used the solvent-accessible surface area [45] to quantify chain aggregation. The value $S = S_{\text{T}}/\Sigma_k S_k$ is the ratio of the total exposed surface area of the chain aggregate S_T to the sum of the areas S_{k} of each chain. Accordingly, a value S of 1 indicates that chains were fully dissociated, while a S value near to 0 implies they are associated to form a condensate. Similar to the other observables, S was evaluated separately for adsorbed ($z \leq 2\sigma$) and adjacent chains, but also for bulk chains ($2\sigma < z \leq L_z$).

Surface area exposure

The total exposed area S_{T} of the tethered chains was also normalized by the number of tethered chains N_{tet}, $S_{\text{c}} = S_T/N_{\text{tet}}$, to obtain the amount of exposed area of each individual chain. Time averages $\langle S_{\text{c}} \rangle_{\text{tet}}$ were computed. $\langle S_{\text{c}} \rangle_{\text{tet}}$ was computed for two different CG resolutions: one bead representing either one VWF protein domain or a VWF monomer. For the latter, the BD trajectories (at the protein-domain level of resolution) were mapped to a monomer-level of resolution by computing the trajectory of the center of masses of the monomers (10 monomers for each chain). The monomer bead radius was estimated to be 10 nm, according to the radial distribution function of the center of masses of the monomers (see results below). Either the protein domain size (a) or the VWF monomer dimension (10 nm) were used as a probe radius for the calculation of S_T and S_{c}. To compare the exposures to the chain extension, both exposure and extension were normalized by the maxima $\langle S_{\text{c}} \rangle_{\text{tet}}^{\text{max}}$ and $\langle r_g^2 \rangle_{\text{tet}}^{\text{max}}$, respectively.

Error estimation

Standard errors were obtained as $SD/\sqrt{n}$, with SD the standard deviation of the computed quantities and n the number of data samples. n was either the number n_t of uncorrelated samples from the time series or the number n_s of chains for the calculation of the chain extension. In the case of the number of adsorbed chains, bootstrapping was used to estimate the error. Accordingly, the time T was divided into 5000 segments. The segments were combined randomly allowing replacement, to obtain $\langle N_{\text{ret}} \rangle$ in ten runs. The error was estimated as the standard deviation of these ten values.

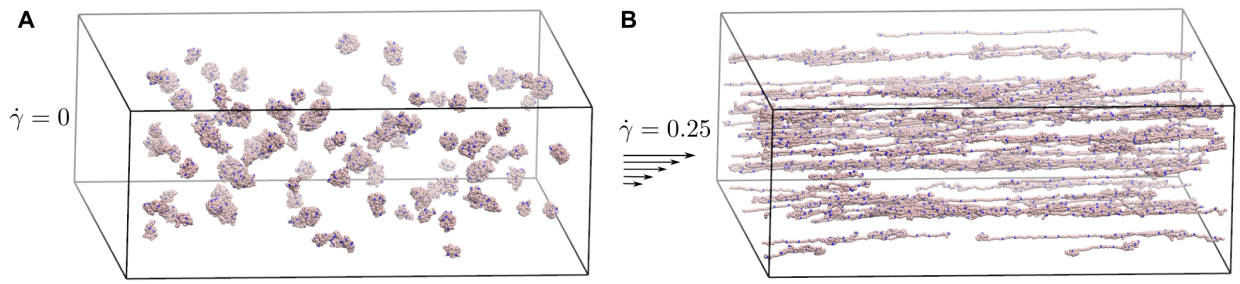

Figure 2: **Brownian dynamics simulations of multi-chain VWF-like biopolymers.** Examples of the final conformations at two typical conditions, at equilibrium conditions in the absence of flow, $\tau\dot{\gamma} = 0$ (A: compact conformations) or in the presence of a moderate shear rate $\tau\dot{\gamma}$ =0.25 (B: stretched conformations).

Results

We used Brownian dynamics simulations to monitor the dynamics of linear biopolymers in the presence of an external shear flow. The biopolymers were modeled as linear bead-spring chains and mimicked the behavior of the multi-domain protein von Willebrand factor.

In our analysis, we distinguished chains that were freely flowing from those that were adsorbed and tethered to the surface. We quantified the distribution of the chain center of mass positions along the Z coordinate (perpendicular to the direction of flow) (Fig. S1). Based on this histogram we defined the height $Z_{\text{cutoff}} \sim 7.12\times10^{-2}$, normalized by the box size (which is equivalent to $6.72\,\sigma$) as the cutoff to define tethered ($Z \leq Z_{\text{cutoff}}$) and bulk ($Z > Z_{\text{cutoff}}$) regions. Accordingly, at that height, the interaction of chains with the surface is negligible, $U_w(6.72\sigma) = -1.5 \times 10^{-3}\epsilon_w$.

Figure 2 shows examples of final conformations obtained by Brownian dynamics simulations in two typical situations, e.g. in the absence of ($\tau\dot{\gamma} = 0$, Fig. 2A) or in the presence of a moderate flow ($\tau\dot{\gamma} = 0.25$, Fig. 2B), respectively. In the absence of flow, the chains adopted a compact configuration. On the contrary, as a consequence of the flow, the shear stress overcame the cohesion forces and the chains stretched along the shear direction rather independently of their initial degree of extension. In addition, chains were adsorbed onto the surface. Furthermore, they formed flowing or tethered conglomerates. In the following sections, we systematically analyze these three different processes, i.e. extension, adsorption, and aggregation, their dependence on the shear flow, and their relevance for the function of the Von Willebrand factor.

Extension

First, we validated our simulation protocol by comparing the dynamics of single chains with previous theoretical and simulation estimates. In the absence of flow, chains in groups displayed an extension $\langle r_{g_0}^2 \rangle$ in the range from 0.152–0.182 (Fig. S2A), while the extension of a single isolated chain, $r_{g_0,s}^2$, varied from 0.150 to 0.264 (Fig. S3). These values are similar to the extension of an ideal chain [46], i.e. $\left\langle R_g^2 \right\rangle / nl^2 \sim 0.167$. The flow dramatically increased the extension, both of a single chain or a concentrate of them (Fig. 3A–B). In particular, for a single bulk chain with a cohesion strength of $\tilde{\epsilon} = 0.4$ and in the presence of a flow of $\tau\dot{\gamma}$=0.67, $r_{g,s}^2$ was found to be ~ 6 (Fig. 3A). This means $\langle R \rangle / (2na) \sim 0.533$, a normalized extension that compares well with previous estimates for similar shear and cohesion values ($\sim$ 0.54–0.56) [4].

Next, we compared the dynamics of a single chain (Fig. 3A) with that of a group of chains (Fig. 3B). As expected for the explored ranges of rates ($\tau\dot{\gamma}$ from 0.1–1.5) and chain cohesion strengths ($\tilde{\epsilon}$ from 0.2–1.0), a monotonic increment in the extension was observed when augmenting the shear flow [4]. The cohesion energy shifted down this increase, although less notoriously for single chains than for interacting ones (compare Fig.s 3A–B). To better quantify the collective behavior of the chains, we monitored the ratio between the chain extension for the multi-chain and the single-chain systems, $\left\langle r_g^2 \right\rangle / r_{g,s}^2$ in Fig. 3C. In the presence of flow, bulk chains were found to elongate almost equally, regardless of whether they were in isolation or in groups (values of around 1 for $\tau\dot{\gamma} > 0$ in Fig. 3C, left panel). On the contrary, at shear rate zero, inter-chain interactions promoted a more extended conformation of the bulk interacting chains (see ratio larger than 1 for $\tau\dot{\gamma} = 0$ in Fig. 3C, left panel). Interestingly, for groups of chains tethered to the surface, the extension was more enhanced compared to the extension of an isolated chain, and this time not only without the shear but also for other small shear-rate values (Fig. 3C, two middle and right panels). As a consequence, in groups, VWF-like biopolymer chains display a different flow-induced elongation propensity, compared to when they are in isolation.

We also checked the impact tethering has on the extension of the interacting chains. For this, we assessed the extension of the tethered chains with respect to the freely bulk flowing ones (Fig. 3D). For low and medium surface-chain interaction strengths, tethered chains stretched to the same extent as the bulk flowing ones (ratios around 1 for $\tilde{\epsilon}_w$ =2 and 6 in Fig. 3D), although with more variability, due to the chain cohesiveness, for zero shear or low-shear values (compare variations in the ratio for low, $\tau\dot{\gamma} < 0.5$, and

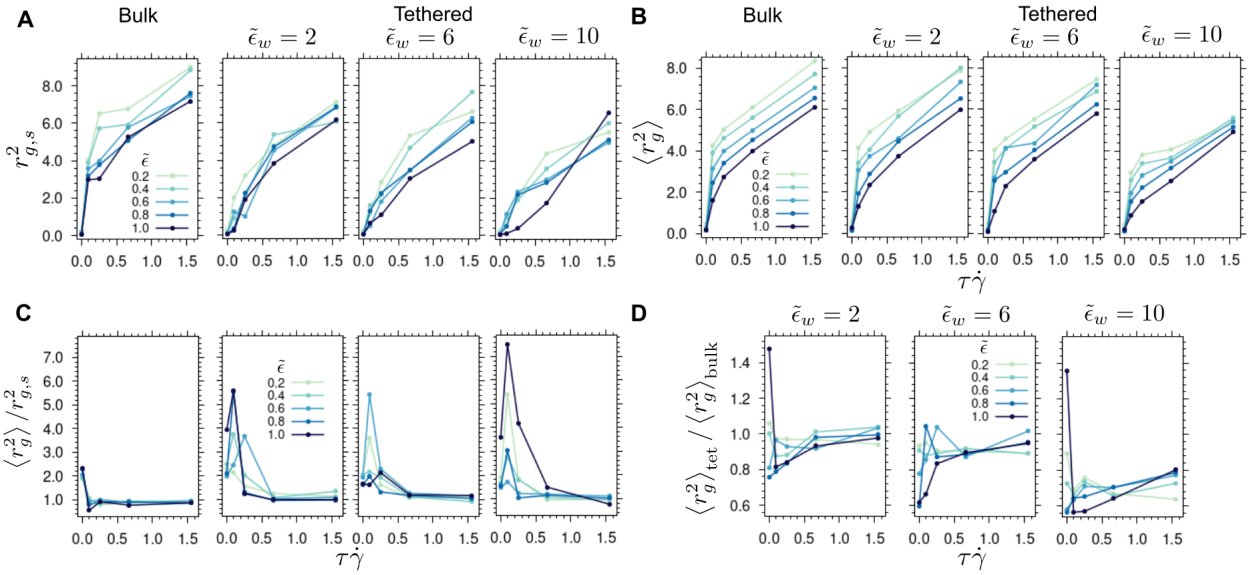

Figure 3: **Extension of VWF-like biopolymers under shear flow.** (A–B) Normalized mean square radius of gyration (r_g^2) for a single chain in isolation (A) or in a multi-chain system (B) as a function of the shear rate ($\tau\dot{\gamma}$), for different polymer–polymer cohesion $\tilde{\epsilon}$ (color) and polymer–surface $\tilde{\epsilon}_w$ (panels) energies. The calculation was carried out for both bulk (left panel) and tethered (two middle and right panels) regions. $\langle\rangle$ denotes the average over chains. Note that in the bulk case, simulations with different $\tilde{\epsilon}_w$ yielded almost identical results (Fig. S4) and thus were averaged into a single curve. The maximum standard error in A was ~ 2.64 and in B it was ~ 0.554 (see errors in detail in Fig. S5). (C) Ratio between the average extension of a chain in the system with multiple chains and that of one chain in isolation, $\langle r_g^2 \rangle / r_{g,s}^2$ (same format as in A and B). (D) Ratio between the extension of tethered chains and that of bulk chains in the multi-chain system: $\langle r_g^2 \rangle_{\text{tet}} / \langle r_g^2 \rangle_{\text{bulk}}$ (same format as in A and B).

large fluxes, $\tau\dot{\gamma} > 0.5$ in Fig. 3D). On the other hand, for a high chain-surface interaction ($\tilde{\epsilon}_w = 10$), the tethered chains were observed to stretch significantly less than their bulk counterparts, pretty much independently of the internal chain cohesion strength (see the right panel in Fig. 3D and Fig. S2B). Thus, chain cohesiveness together with surface adhesiveness non-trivially modulate the extension of groups of chains.

Adsorption and Tethering

We next investigated the spontaneous adsorption and posterior tethering of the chains. Fig. 4A shows the number of tethered chains as a function of time for all 75 simulations we carried out, which drastically varied depending on the applied flow, and the chain–chain cohesion and chain–surface interaction energies. We considered the mean $\langle N_{\text{tet}} \rangle$ to quantify the overall adhesion to the surface. As expected, the number of tethered chains increased as the chain–surface interaction energy augmented (Fig. 4B). For each of such energies, the shear flow caused a reduction in $\langle N_{\text{tet}} \rangle$ (Fig. 4B). No clear trend with the cohesion energy $\tilde{\epsilon}$ was observed, although it is interesting to note that a large variability between the curves for the different cohesion values (variations in $\tilde{\epsilon}$) was observed as the surface adhesion energy $\tilde{\epsilon}_w$ increased (Fig. 4B).

Interestingly, adsorbed chains also formed aggregates with other adjacent chains which were not in direct contact with the surface. Accordingly, sequences of secondary chains tethered to the surface were established (Fig. 4C). States with multiple adjacent chains were rather short-lived and they mainly consisted of the second layer of neighbors(Fig. S7). The probability P_{adj} of observing at least one adjacent chain was especially high, and P_{adj} increased as cohesion augmented, for moderate chain–surface interaction energies and flows (Fig. 4D).

Thus, the chain–surface energy and the strength of the shear flow largely dominate the amount of tethered chains. In turn, cohesion between chains plays a minor but still noticeable distorting role, contributing to the cooperative tethering of secondary chains.

Aggregation

We continued our study by analyzing the way chains aggregated with each other. As a measure of aggregation, we used the quantity S which is defined as the solvent-accessible surface area of all polymer chains together, divided by the sum of the areas of the individual chains (see methods). The highest possible aggregation was obtained in the absence of flow (see lowest values of S below one in figure 5). Augmenting the flow, mostly diminished the level aggregation (increase $\langle S \rangle$ to values near one) in a

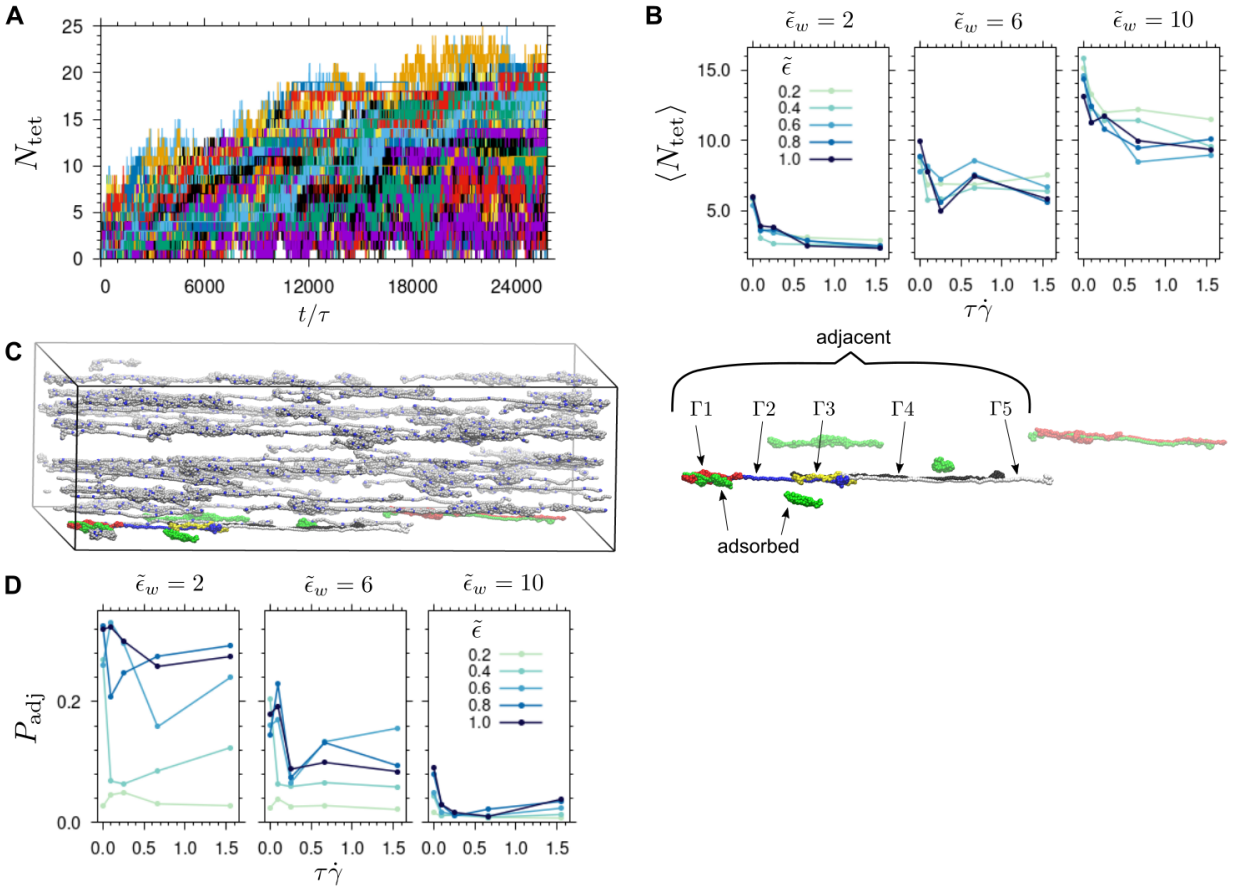

Figure 4: **Adsorption and tethering of VWF-like biopolymers under shear flow recovered from BD simulations**. (A) The number N_{tet} of chains tethered to the surface is displayed as a function of time (in τ units) for all 75 carried-out simulations. $N_{\text{tet}} = N_{\text{ads}} + N_{\text{adj}}$, including the number of adsorbed chains N_{ads} and of adjacently immobilized chains N_{adj}, i.e. the chains that were in contact with the adsorbed chains but not in direct contact with the surface. (B) Mean of N_{tet} as function of the shear flow $\tau\dot{\gamma}$, and the polymer–polymer cohesion $\tilde{\epsilon}$ (color) and the polymer-surface $\tilde{\epsilon}_w$ interaction (panels). The maximum value of the error in $\langle N_{\text{tet}} \rangle$ was estimated by bootstrapping to be 0.1 (Fig. S6A). (C) The snapshot highlights the tethered chains (color) and the bulk ones (gray), and indicates the different types (Γ from 1-5) of adjacent chains, sequentially tethered to one adsorbed chain. (D) Probability P_{adj} of observing at least one adjacent chain attached to an adsorbed chain as a function of the shear flow $\tau\dot{\gamma}$, the chain-chain cohesion $\tilde{\epsilon}$ (color) and the chain-surface interaction $\tilde{\epsilon}_w$ (panels) (same format as in B).

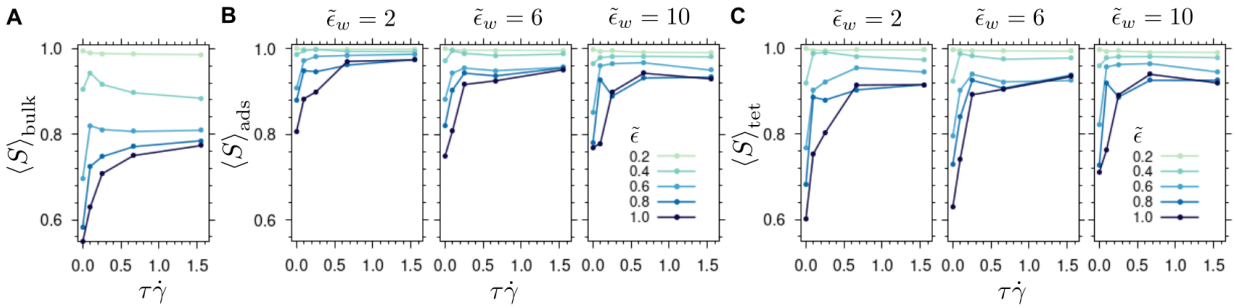

Figure 5: **Aggregation of biopolymer VWF-like chains recovered from the simulations**. Time-averaged weighted surface exposure ratio, $\langle S \rangle$, for bulk (A), adsorbed (B), and tethered chains (C) is presented as a function of the shear rate ($\tau\dot{\gamma}$), the polymer cohesion $\tilde{\epsilon}$ (color) and polymer–surface interaction strength $\tilde{\epsilon}_w$ (panels). Note that $\langle S \rangle_{\text{bulk}}$ was found to be practically invariant to changes in $\tilde{\epsilon}_w$ (Fig. S8). Accordingly, here, the average between the values obtained for three different energies $\tilde{\epsilon}_w$ is shown. The maximum standard error of S was 0.039 (A), 0.146 (B), and 0.127 (C)(see errors in detail in Fig. S9).

hyperbolic fashion. This trend was tuned by the cohesion energy $\tilde{\epsilon}$, rather independently of whether the chains were bulk or tethered ones (Fig. 5).

Together, cohesion and adsorption strengths induced intriguing behaviors described as follows. Bulk chains were largely influenced by the cohesion energy $\tilde{\epsilon}$ (Fig. 5A), displaying a non-monotonic reducing aggregation dependence on the flow for intermediate cohesion values ($\tilde{\epsilon}$=0.4 and 0.6), while increasing monotonically for high values ($\tilde{\epsilon}$=0.8 and 1.0). Adsorbed chains were less susceptible to changes in the cohesion energy and showed less aggregation than the bulk ones (compare Fig.s 5A and 5B). On the other hand, when adjacent chains were also considered, a stronger aggregation response was observed at low flows (compare Fig.s 5B and 5C). This constitutes another indication of the previously-shown, interaction of adjacent chains with the adsorbed ones (see Fig.s 4C–D). Nonetheless, both adsorbed and tethered chains reached a similar aggregation degree for the high considered shear rates (see $\langle S \rangle$ for $\tau\dot{\gamma}$ =0.67 and 1.55 in Fig.s 5B–C), indicating that the cooperative coexistence of tethered aggregates occurred principally at low values of flow. Interestingly, the interaction energy with the surface had a rather moderate influence on the adsorbed chains (i.e. in direct contact with the surface) but a notable diminishing effect in the aggregation of the tethered ones (i.e. including the adjacent chains too) (compare distinct $\tilde{\epsilon}_w$ in Fig.s 5B–C).

In summary, aggregation is largely modulated by the cohesion between chains and the shear flow. The interaction of the chains with the surface also influences this process, by altering the aggregation of chains that are not in direct contact with the surface.

Receptor density

The receptor density on the surface, φ, is unknown. The collagen I surface density of $7.5 \cdot 10^{-4}$ molecules/nm^2 [47] may be considered as a lower boundary because each collagen I molecule could provide multiple receptor sites. In our simulations, we set $\varphi = 10^{-2}$ nm^{-2}, which corresponds roughly to one receptor in a squared area covered by one globular VWF monomer (given that the radius of a VWF monomer is $\sim$10 nm, see below). We considered this density to sample a sufficient number of adsorption events while avoiding the formation of an exclusion region. (Fig S10). Note that the extension and aggregation of the bound chains did not drastically change when decreasing the density by a factor of ten, closer to the density used in a previous study of about 1/8 receptors per monomer area [39] (Fig. S11).

Chain surface exposure

The extension of the chains has been typically considered as the main descriptor of VWF shear-response. However, the protein surface area exposed to the solvent is a quantity that is closer to the main physiological action of the flow on VWF, namely, exposing cryptic binding sites to enable the interaction of VWF with its partners, such as collagen or platelets. We thus took advantage of the surface area calculations to investigate the actual level of exposure of the VWF chains.

At a level of resolution of one bead representing a protein domain, the recovered surface exposure area of all tethered chains together $\langle S_c \rangle_{\text{tet}}$ varied from 2×10^3 nm^2 (in the absence of flow) to areas of roughly 7×10^3 nm^2 (Fig. 6A). By mapping the conformations into a lower resolution model, in which one bead represents a monomer (i.e. 12 protein-domain beads), exposure values were up to five-fold higher (Fig. 6B). At both resolutions, the surface area increased with the flow and decreased with the cohesion energy in a monotonic fashion (Fig. 6A–B). However, at the monomer level of resolution, a stronger dependence on $\tilde{\epsilon}_w$ was obtained (Fig. 6B). We compared the exposed surface area with the extension of Fig. 3B (two middle and right panels) in figures 6C–D. Exposed surface areas grew suddenly as the flow increased, i.e. high degrees of exposure were already obtained at small flow values, while

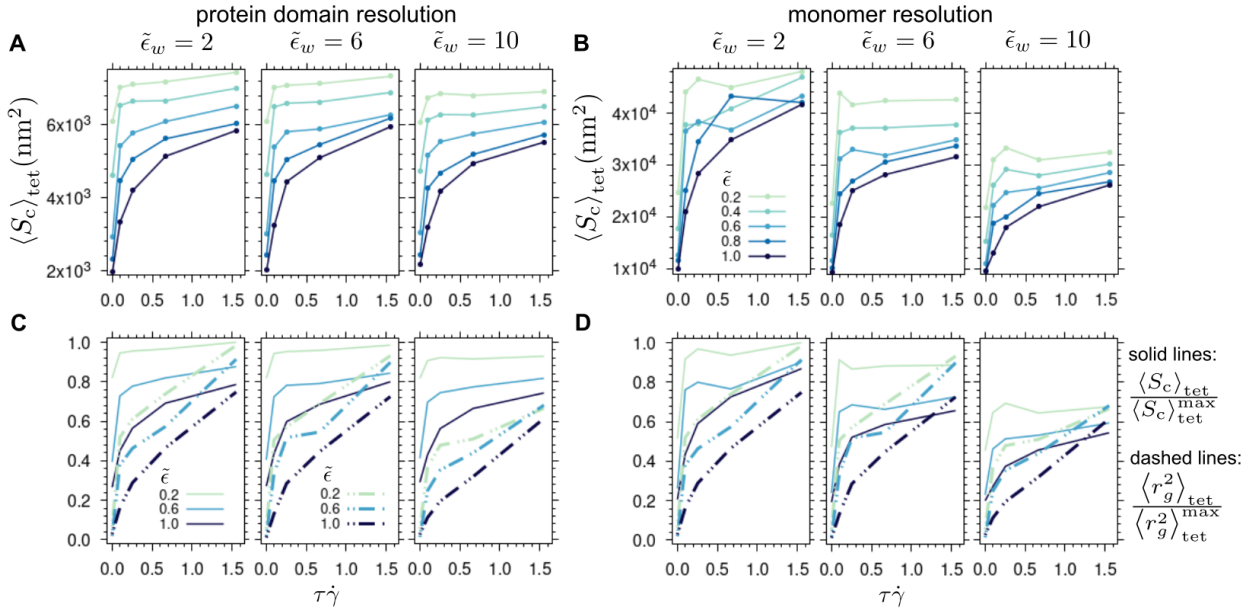

Figure 6: **Surface exposure of biopolymer VWF-like chains**. (A–B) Time-averaged surface exposure of all tethered chains together ($\langle S_s \rangle_{\rm tet}$) was computed at a level of resolution of one bead representing a protein domain (A) and a bead corresponding to a monomer, i.e. 12 beads (B). Exposure was computed as function of the shear rate ($\tau\dot{\gamma}$), the chain-chain cohesion $\tilde{\epsilon}$ (color), and chain-surface interaction $\tilde{\epsilon}_w$ (panels) strengths. (C–D) Normalized exposures (solid lines from A and B) are compared to normalized chain extensions (dashed lines, extracted from Fig. 3B, two middle and right panels) for both levels of resolution. The highest observed value from all the simulations was considered as the normalization factor. The same format is used as in A and B. Plots for $\tilde{\epsilon}$=0.4 and $\tilde{\epsilon}$=0.6 were omitted for clarity. The maximum value of the standard error in S_c was 903 nm^2 (see errors in detail in Fig. S6B).

the extension augmented more gradually with the flow (Fig.s. 6C-D). Accordingly, the correlation between the exposed area and the extension is not trivial. Remarkably, the exposure at the domain level is almost non-sensitive to the chain-surface interaction energy (Fig. 6C). In contrast, at the monomer level, it exhibits a similar attenuation with this energy as the extension (Fig. 6D). Thus the adopted level of resolution impacts the surface area chains expose in dependency on the surface adhesion energy.

Discussion

Here, we used Brownian dynamics simulations to systematically examine the elongation, adsorption, aggregation, and surface exposure of biopolymers that resembled the extracellular blood protein VWF under shear flows.

By means of a parameter exploration, we retrieved different regimes in which intra- or inter-chain cohesion, together with the adhesiveness to the surface, modulated the response to shear flow. Overall, there is no dominant factor, but it is the coexistence between them that dictates the chain behavior. For instance, the extension was not only influenced by the cohesion between chains but also by the interaction of them with the surface, i.e. the stronger the latter the more compact chains were (Fig. 3B). Reciprocally, the adsorption of chains was mainly modulated by their interaction with the surface but the cohesive interactions between beads distorted this trend (Fig. 4B), promoting secondary tethering (Fig.s 4C–D). Accordingly, at the low flow values studied here, both the chain cohesiveness and the interaction with the surface promoted the aggregation of tethered chains, of relevance for the VWF function (Fig.s 5B–C). Full phase diagrams had been previously determined for homo-polymers that adsorbed on homogeneous and non-homogeneous surfaces [33, 34]. Accordingly, our findings expand these studies by describing the complex interplay between chain-chain cohesion and chain-surface adhesion that influence the response of VWF to shear.

Self-association is a key feature for VWF function [20, 15, 16, 17, 23]. Self-association has the advantage of providing more adhesion sites to platelets, through indirectly immobilizing VWF chains [18]. Our results provide evidence of the spontaneous immobilization of self-associated VWF-like biopolymers (Fig.s 4–5). Our work quantifies the build-up of functionally absorbed aggregates in response flows at different cohesion/adsorption regimes and it thereby supports the notion of cooperative adsorption previously described for VWF [39].

Our work also compared the collective behavior of the polymer chains. Interestingly, for tethered chains at moderately-low flows, inter-chain interactions out-competed intra-

chain ones resulting in a higher elongation of chains within an aggregate than in isolation (Fig.s. 3A–C). Furthermore, the elongation of tethered chains was similar to that of freely flowing bulk ones, except for chains that strongly interacted with the surface and thereby were less extended (Fig. 3D). Note that the term "tethered" conventionally refers to an end-attached polymer [20, 48]. In that case, tethered chains elongate more than bulk chains [49]. Here, we did not covalently immobilize the chains (as it has been done experimentally [22, 20]) but rather let them spontaneously bind to the surface, as it may be more likely to occur physiologically. A consequence of the multiple interaction points each VWF chain contains is that the strength of the interaction impacts the elongation of the chains deposited on the surface [41]. Hence, here we stress additional elongation properties that emerge when considering collectively multivalent adherent chains.

In our model, we adopted a CG resolution of one protein domain represented by one bead, as previously done to study D4-D4 interactions [40]. This level of resolution allowed us to take into account a more realistic distribution of adhesion points (corresponding to the VWF A3 domain). Surprisingly, the exposure did not significantly reduce when the interaction with the surface increased as it was observed for the chain elongation (Fig.s 6A,C). VWF has been commonly simulated at a lower level of resolution, typically one VWF monomer or dimer being represented by one or two beads [4, 33, 34, 40, 39, 35, 48, 38, 42]. When mapping our results to that low level of resolution, the surface area exposed to the solvent is much more sensitive to the interaction with the surface and correlates better with the trend exhibited by the chain elongation (Figure 6B,D). The exposed surface area is an essential functional quantity as it relates to the binding sites which are effectively available for the interaction of VWF with its partners, which are otherwise cryptic in the absence of shear. Conventionally, elongation is taken as a proxy for this observable. Our results confirm that qualitatively the correlation between elongation and surface exposure holds well, i.e. the more elongated the chains the more of the exposed area is available, but they more quantitatively coincide at a VWF-monomer size level of resolution. Ours constitutes an approach to connect fine-grain protein-domain details into coarser descriptions of VWF.

Conclusion

Here, we studied the dynamics of polymers that resembled the blood protein VWF under shear flows by using Brownian dynamics simulations. Our simulations quantify the effect polymer-polymer cohesive and polymer-surface adhesion forces have on the flow-induced shear response of VWF. These forces coexist non-trivially to tune the elongation propensity of VWF and the formation of functional adsorbed VWF aggregates. Our data emphasizes the collective behavior of such aggregates featuring additional properties that VWF chains do not exhibit in isolation or freely flowing. Finally, we show that the resolution of the coarse-grain model impacts the exposed area of VWF aggregates. This systematic study is expected to contribute to our understanding of VWF and its ability to self-associate to accomplish its key hemostatic function.

Author Contributions

H.A.-E. carried out the simulations. A.A.-K. and C.A.-S. designed the research. All authors analyzed the data and wrote the article.

Acknowledgements

We thank Juan Carlos Briceño for the helpful discussions. For their funding, we are also grateful to the Max Planck Tandem initiative at the Universidad de los Andes (to H.A.-E and C.A.-S), the MIT International Science and Technology Initiatives (MISTI) Global Seed Funds (all authors), and to the Klaus Tschira Foundation (to C.A.-S.). We thank Frauke Gräter for the Ph.D. student internship (to H.A.-E.). We thank Guy Henderson for carefully reading the manuscript. We acknowledge the Max Planck Computing & Data Facility in Garching, Germany, and the HPC data center of the Universidad de los Andes in Bogota, Colombia, for the computing time and computational resources.

References

[1] Timothy A. Springer. von Willebrand factor, Jedi knight of the bloodstream. *Blood*, 124(9):1412–1425, August 2014.

[2] Gui-Ping Luo, Bing Ni, Xia Yang, and Yu-Zhang Wu. von Willebrand Factor: More Than a Regulator of Hemostasis and Thrombosis. *Acta Haematol*, 128(3):158–169, 2012.

[3] Denisa D. Wagner. Cell Biology of von Willebrand Factor. *Annu. Rev. Cell. Biol.*, 6(1):217–242, November 1990.

[4] A. Alexander-Katz, M. F. Schneider, S. W. Schneider, A. Wixforth, and R. R. Netz. Shear-Flow-Induced Unfolding of Polymeric Globules. *Phys. Rev. Lett.*, 97(13):138101, September 2006.

[5] S. W. Schneider, S. Nuschele, A. Wixforth, C. Gorzelanny, A. Alexander-Katz, R. R. Netz, and M. F. Schneider. Shear-induced unfolding triggers adhesion of von Willebrand factor fibers. *Proceedings of the National Academy of Sciences*, 104(19):7899–7903, May 2007.

[6] Hsieh Chen, Mohammad A. Fallah, Volker Huck, Jennifer I. Angerer, Armin J. Reininger, Stefan W. Schneider, Matthias F. Schneider, and Alfredo Alexander-Katz. Blood-clotting-inspired reversible polymer-colloid composite assembly in flow. *Nat Commun*, 4(1):1333, June 2013.

[7] Marijke Bryckaert, Jean-Philippe Rosa, Cécile V. Denis, and Peter J. Lenting. Of von Willebrand factor and platelets. *Cell. Mol. Life Sci.*, 72(2):307–326, January 2015.

[8] J. Evan Sadler. Biochemistry and genetics of von Willebrand Factor. *Annu. Rev. Biochem.*, 67(1):395–424, June 1998.

[9] R. Schneppenheim and U. Budde. von Willebrand factor: the complex molecular genetics of a multidomain and multifunctional protein: Molecular genetics of a multidomain and multifunctional protein. *Journal of Thrombosis and Haemostasis*, 9:209–215, July 2011.

[10] Ernest T. Parker and Pete Lollar. Conformation of the von Willebrand factor/factor VIII complex in quasi-static flow. *Journal of Biological Chemistry*, 296:100420, January 2021.

[11] Svenja Lippok, Tobias Obser, Jochen P. Müller, Valentin K. Stierle, Martin Benoit, Ulrich Budde, Reinhard Schneppenheim, and Joachim O. Rädler. Exponential Size Distribution of von Willebrand Factor. *Biophysical Journal*, 105(5):1208–1216, September 2013.

[12] T. H. C. Brondijk, D. Bihan, R. W. Farndale, and E. G. Huizinga. Implications for collagen I chain registry from the structure of the collagen von Willebrand factor A3 domain complex. *Proceedings of the National Academy of Sciences*, 109(14):5253–5258, April 2012.

[13] John J. Dumas, Ravindra Kumar, Thomas McDonagh, Francis Sullivan, Mark L. Stahl, William S. Somers, and Lidia Mosyak. Crystal Structure of the Wild-type von Willebrand Factor A1-Glycoprotein Ibα Complex Reveals Conformation Differences with a Complex Bearing von Willebrand Disease Mutations. *Journal of Biological Chemistry*, 279(22):23327–23334, May 2004.

[14] Eric G. Huizinga, Shizuko Tsuji, Roland A. P. Romijn, Marion E. Schiphorst, Philip G. de Groot, Jan J. Sixma, and Piet Gros. Structures of Glycoprotein Ibα and Its Complex with von Willebrand Factor A1 Domain. *Science*, 297(5584):1176–1179, August 2002.

[15] Brian Savage, Jan J. Sixma, and Zaverio M. Ruggeri. Functional self-association of von Willebrand factor during platelet adhesion under flow. *Proc. Natl. Acad. Sci. U.S.A.*, 99(1):425–430, January 2002.

[16] Harish Shankaran, Paschalis Alexandridis, and Sriram Neelamegham. Aspects of hydrodynamic shear regulating shear-induced platelet activation and self-association of von Willebrand factor in suspension. *Blood*, 101(7):2637–2645, April 2003.

[17] Alexej Barg, Rainer Ossig, Tobias Goerge, Matthias Schneider, Hermann Schillers, Hans Oberleithner, and Stefan Schneider. Soluble plasma-derived von Willebrand factor assembles to a haemostatically active filamentous network. *Thromb Haemost*, 97(04):514–526, 2007.

[18] José A. López and Dominic W. Chung. VWF self-association: more bands for the buck. *Blood*, 116(19):3693–3694, November 2010.

[19] Kannayakanahalli M. Dayananda, Indrajeet Singh, Nandini Mondal, and Sriram Neelamegham. von Willebrand factor self-association on platelet GpIbα under hydrodynamic shear: effect on shear-induced platelet activation. *Blood*, 116(19):3990–3998, November 2010.

[20] Hongxia Fu, Yan Jiang, Wesley P. Wong, and Timothy A. Springer. Single-molecule imaging of von Willebrand factor reveals tension-dependent self-association. *Blood*, 138(23):2425–2434, December 2021.

[21] H. Ulrichts, K. Vanhoorelbeke, J. P. Girma, P. J. Lenting, S. Vauterin, and H. Deckmyn. The von Willebrand factor self-association is modulated by a multiple domain interaction. *J Thromb Haemost*, 3(3):552–561, March 2005.

[22] Matthias F. Schneider, Mohammad A. Fallah, Christian Mess, Tobias Obser, Reinhard Schneppenheim, Alfredo Alexander-Katz, Stefan W. Schneider, and Volker Huck. Platelet adhesion and aggregate formation controlled by immobilised and soluble VWF. *BMC Mol and Cell Biol*, 21(1):64, December 2020.

[23] Changjie Zhang, Anju Kelkar, and Sriram Neelamegham. von Willebrand factor self-association is regulated by the shear-dependent unfolding of the A2 domain. *Blood Advances*, 3(7):957–968, April 2019.

[24] Diego Butera, Freda Passam, Lining Ju, Kristina M. Cook, Heng Woon, Camilo Aponte-Santamaría, Elizabeth Gardiner, Amanda K. Davis, Deirdre A. Murphy, Agnieszka Bronowska, Brenda M. Luken, Carsten Baldauf, Shaun Jackson, Robert Andrews, Frauke Gräter, and Philip J. Hogg. Autoregulation of von Willebrand factor function by a disulfide bond switch. *Sci. Adv.*, 4(2):eaaq1477, February 2018.

[25] C. Martin, L. D. Morales, and M. A. Cruz. Purified A2 domain of von Willebrand factor binds to the active conformation of von Willebrand factor and blocks the interaction with platelet glycoprotein Ibα. *J Thromb Haemost*, 5(7):1363–1370, July 2007.

[26] Camilo Aponte-Santamaría, Volker Huck, Sandra Posch, Agnieszka K. Bronowska, Sandra Grässle, Maria A. Brehm, Tobias Obser, Reinhard Schneppenheim, Peter Hinterdorfer, Stefan W. Schneider, Carsten Baldauf, and Frauke Gräter. Force-Sensitive Autoinhibition of the von Willebrand Factor Is Mediated by Interdomain Interactions. *Biophysical Journal*, 108(9):2312–2321, May 2015.

[27] Sandra Posch, Camilo Aponte-Santamaría, Richard Schwarzl, Andreas Karner, Matthias Radtke, Frauke Gräter, Tobias Obser, Gesa König, Maria A. Brehm,

Hermann J. Gruber, Roland R. Netz, Carsten Baldauf, Reinhard Schneppenheim, Robert Tampé, and Peter Hinterdorfer. Mutual A domain interactions in the force sensing protein von Willebrand factor. *Journal of Structural Biology*, 197(1):57–64, January 2017.

[28] Jochen P. Müller, Salomé Mielke, Achim Löf, Tobias Obser, Christof Beer, Linda K. Bruetzel, Diana A. Pippig, Willem Vanderlinden, Jan Lipfert, Reinhard Schneppenheim, and Martin Benoit. Force sensing by the vascular protein von Willebrand factor is tuned by a strong intermonomer interaction. *Proc Natl Acad Sci USA*, 113(5):1208–1213, February 2016.

[29] Zimei Shu, Jianwei Zeng, Li Xia, Haiyan Cai, and Aiwu Zhou. Structural mechanism of VWF D'D3 dimer formation. *Cell Discov*, 8(1):14, December 2022.

[30] Jianwei Zeng, Zimei Shu, Qian Liang, Jing Zhang, Wenman Wu, Xuefeng Wang, and Aiwu Zhou. Structural basis of von Willebrand factor multimerization and tubular storage. *Blood*, 139(22):3314–3324, June 2022.

[31] Gabriel Javitt and Deborah Fass. Helical self-assembly of a mucin segment suggests an evolutionary origin for von Willebrand factor tubules. *Proc. Natl. Acad. Sci. U.S.A.*, 119(15):e2116790119, April 2022.

[32] Jacob Ronald Anderson, Jing Li, Timothy A. Springer, and Alan Brown. Structures of VWF tubules before and after concatemerization reveal a mechanism of disulfide bond exchange. *Blood*, page blood.2022016467, July 2022.

[33] Matthias Radtke, M Radtke, and R. Netz. Shear-induced dynamics of polymeric globules at adsorbing homogeneous and inhomogeneous surfaces. *Eur. Phys. J. E*, 37(3):20, March 2014.

[34] Matthias Radtke and Roland R. Netz. Shear-enhanced adsorption of a homopolymeric globule mediated by surface catch bonds. *Eur. Phys. J. E*, 38(6):69, June 2015.

[35] Masoud Hoore, Kathrin Rack, Dmitry A Fedosov, and Gerhard Gompper. Flow-induced adhesion of shear-activated polymers to a substrate. *J. Phys.: Condens. Matter*, 30(6):064001, February 2018.

[36] Yulia K. Kushchenko and Aleksey V. Belyaev. Effects of hydrophobicity, tethering and size on flow-induced activation of von Willebrand factor multimers. *Journal of Theoretical Biology*, 485:110050, January 2020.

[37] Svenja Lippok, Matthias Radtke, Tobias Obser, Lars Kleemeier, Reinhard Schneppenheim, Ulrich Budde, Roland R. Netz, and Joachim O. Raedler. Shear-Induced Unfolding and Enzymatic Cleavage of Full-Length VWF Multimers. *Biophysical Journal*, 110(3):545–554, February 2016.

[38] Sagar Kania, Alparslan Oztekin, Xuanhong Cheng, X. Frank Zhang, and Edmund Webb. Predicting pathological von Willebrand factor unraveling in elongational flow. *Biophysical Journal*, 120(10):1903–1915, May 2021.

[39] Maziar Heidari, Mehrdad Mehrbod, Mohammad Reza Ejtehadi, and Mohammad R. K. Mofrad. Cooperation within von Willebrand factors enhances adsorption mechanism. *Journal of The Royal Society Interface*, 12(109):20150334, August 2015.

[40] Aleksey V. Belyaev. Intradimer forces and their implication for conformations of von Willebrand factor multimers. *Biophysical Journal*, 120(5):899–911, March 2021.

[41] Andrey Milchev and Kurt Binder. Linear Dimensions of Adsorbed Semiflexible Polymers: What Can Be Learned about Their Persistence Length? *Phys. Rev. Lett.*, 123(12):128003, September 2019.

[42] Wei Wei, Chuqiao Dong, Michael Morabito, Xuanhong Cheng, X. Frank Zhang, Edmund B. Webb, and Alparslan Oztekin. Coarse-Grain Modeling of Shear-Induced Binding between von Willebrand Factor and Collagen. *Biophysical Journal*, 114(8):1816–1829, April 2018.

[43] Donald L. Ermak and J. A. McCammon. Brownian dynamics with hydrodynamic interactions. *The Journal of Chemical Physics*, 69(4):1352–1360, August 1978.

[44] Berk Hess, Carsten Kutzner, David van der Spoel, and Erik Lindahl. GROMACS 4: Algorithms for Highly Efficient, Load-Balanced, and Scalable Molecular Simulation. *J. Chem. Theory Comput.*, 4(3):435–447, March 2008.

[45] M. L. Connolly. Analytical molecular surface calculation. *J Appl Crystallogr*, 16(5):548–558, October 1983.

[46] Michael Rubinstein and Ralph H. Colby. *Polymer physics*. Oxford University Press, Oxford ; New York, 2003.

[47] Christianne Gaudet, William A. Marganski, Sooyoung Kim, Christopher T. Brown, Vaibhavi Gunderia, Micah Dembo, and Joyce Y. Wong. Influence of Type I Collagen Surface Density on Fibroblast Spreading, Motility, and Contractility. *Biophysical Journal*, 85(5):3329–3335, November 2003.

[48] Yi Wang, Michael Morabito, X. Frank Zhang, Edmund Webb, Alparslan Oztekin, and Xuanhong Cheng. Shear-Induced Extensional Response Behaviors of Tethered von Willebrand Factor. *Biophysical Journal*, 116(11):2092–2102, June 2019.

[49] Richard Schwarzl and Roland Netz. Hydrodynamic Shear Effects on Grafted and Non-Grafted Collapsed Polymers. *Polymers*, 10(8):926, August 2018.